nature physics

LETTERS

https://doi.org/10.1038/s41567-021-01164-9

Check for updates

# A hierarchy of protein patterns robustly decodes cell shape information

Manon C. Wigbers[1,4], Tzer Han Tan[2,4], Fridtjof Brauns[1], Jinghui Liu[2], S. Zachary Swartz[3], Erwin Frey[1]✉ and Nikta Fakhri[2]✉

**Many cellular processes, such as cell division[1–3], cell motility[4], wound healing[5] and tissue folding[6,7], rely on the precise positioning of proteins on the membrane. Such protein patterns emerge from a combination of protein interactions, transport, conformational state changes and chemical reactions at the molecular level[8]. Recent experimental and theoretical work clearly demonstrates the role of geometry, including membrane curvature[9–11] and local cytosolic-to-membrane ratios[12,13], and advective cortical flow in modulating membrane protein patterns. However, it remains unclear how these proteins achieve robust spatiotemporal organization on the membrane during the dynamic cell shape changes involved in physiological processes. Here we use oocytes of the starfish *Patiria miniata* as a model system to elucidate a shape-adaptation mechanism that robustly controls spatiotemporal protein dynamics on the membrane in spite of cell shape deformations. By combining experiments with biophysical theory, we show how cell shape information contained in a cytosolic gradient can be decoded by a bistable regulator of the enzyme Rho, which is associated with contractility. This bistable front in turn controls a mechanochemical response by locally triggering excitable dynamics of Rho. We posit that such a shape-adaptation mechanism based on a hierarchy of protein patterns may constitute a general physical principle for cell shape sensing and control.**

In starfish oocytes, the cell shape is dynamically deformed by surface contraction waves that travel along the membrane from the vegetal pole (VP) to the animal pole (AP) during meiotic anaphase (Fig. 1a,b). Surface contraction waves are observed in many species[14–18], but their functional role is still under debate[19,20]. Recent work[21] has clearly demonstrated that surface contraction waves are induced by the GTPase Rho, which, when GTP-bound, locally triggers actomyosin contractility and thereby generates a zone of surface contraction that travels as a band across the membrane (Fig. 1c and Supplementary Video 1). When the mechanical properties of the oocyte surface are altered by removing the extracellular jelly layer[21], the degree of deformation becomes greater and, remarkably, the surface contraction wave slows down (Fig. 1d). The same effect was observed previously when myosin contractility was increased to amplify shape deformations[22]. These observations establish the starfish oocyte as an ideal model system to unravel the dynamic interplay between cell shape and biochemical dynamics.

To investigate how the Rho dynamics are affected by cell shape, we adopt a strategy established previously[2,21], which is to confine the oocytes in microfabricated chambers of various shapes (Fig. 1e). We find that shape affects both the initiation and the propagation speed of the Rho-GTP band. Specifically, we observe that the Rho-GTP band always initiates from regions of high curvature, which we refer to as 'corners' (Fig. 1f–i and Supplementary Videos 2–5). Moreover, in elliptical (Fig. 1g and Supplementary Fig. 1a,b) and triangular (Fig. 1h and Supplementary Fig. 1c,d) geometries, multiple wave initiations occur, with the first starting from the corner farthest from the nucleus (Fig. 1g,h, c1 label). Interestingly, in the star geometry, wave initiations occur simultaneously from the two corners farthest away from the nucleus (Fig. 1i, c1 and c2 labels, and Supplementary Fig. 1e), even though there are five corners with the same local curvature, which suggests that local mechanics alone are not sufficient to trigger wave initiations. Strikingly, these waves propagate with varying speeds on different sections of the membrane such that they always meet closest to the nucleus (AP). This suggests that wave initiations and propagation are globally coordinated.

Motivated by recent experimental evidence that the Rho-GTP band is guided by a temporally decaying cytosolic gradient of the kinase-active Cdk1-cyclinB complex[21], we hypothesize that Cdk1-cyclinB provides this global coordination, analogous to positional information in morphogenesis[23]. In an unconfined oocyte, the Cdk1-cyclinB forms a cytosolic gradient that is high at the AP and low at the VP[21] (Fig. 1j–l and Supplementary Video 6). To test how cell shape modulates this gradient, we imaged the evolution of the Cdk1-cyclinB concentration gradient (in short, the cytosolic Cdk1 gradient) in different cell shapes (Fig. 1m, Supplementary Fig. 2 and Supplementary Videos 7–9). In all cell shapes tested, this gradient extends radially from the AP into the cytoplasm (Fig. 1j,m and Supplementary Fig. 2). Consequently, the gradient perceived along the membrane (in short, the membrane Cdk1 gradient) depends on the membrane orientation relative to the cytosolic Cdk1 gradient. In an elliptical geometry, the membrane Cdk1 gradient is shallow at the corners (c1 and c2) but steeper in the middle of the elliptically shaped oocyte (Fig. 1m–o). These results demonstrate how the membrane Cdk1 gradient encodes information about cell shape.

In the different cell shapes, the Cdk1-cyclinB concentration is always lowest at the corner farthest away from the nucleus, which precisely coincides with the first wave initiation points (Fig. 1o and Supplementary Fig. 2). In addition, Cdk1-cyclinB concentration forms local minima at other corners, which coincides with subsequent wave initiation points (Fig. 1f–i and Supplementary Fig. 2). This is consistent with previous work that indicates that the Rho-GTP band originates at the point of lowest Cdk1-cyclinB concentration in unconfined oocytes[21]. Furthermore, our experiments

[1]Arnold Sommerfeld Center for Theoretical Physics and Center for NanoScience, Department of Physics, Ludwig Maximilian University of Munich, Munich, Germany. [2]Department of Physics, Massachusetts Institute of Technology, Cambridge, MA, USA. [3]Whitehead Institute for Biomedical Research, Cambridge, MA, USA. [4]These authors contributed equally: Manon C. Wigbers, Tzer Han Tan. ✉e-mail: frey@lmu.de; fakhri@mit.edu

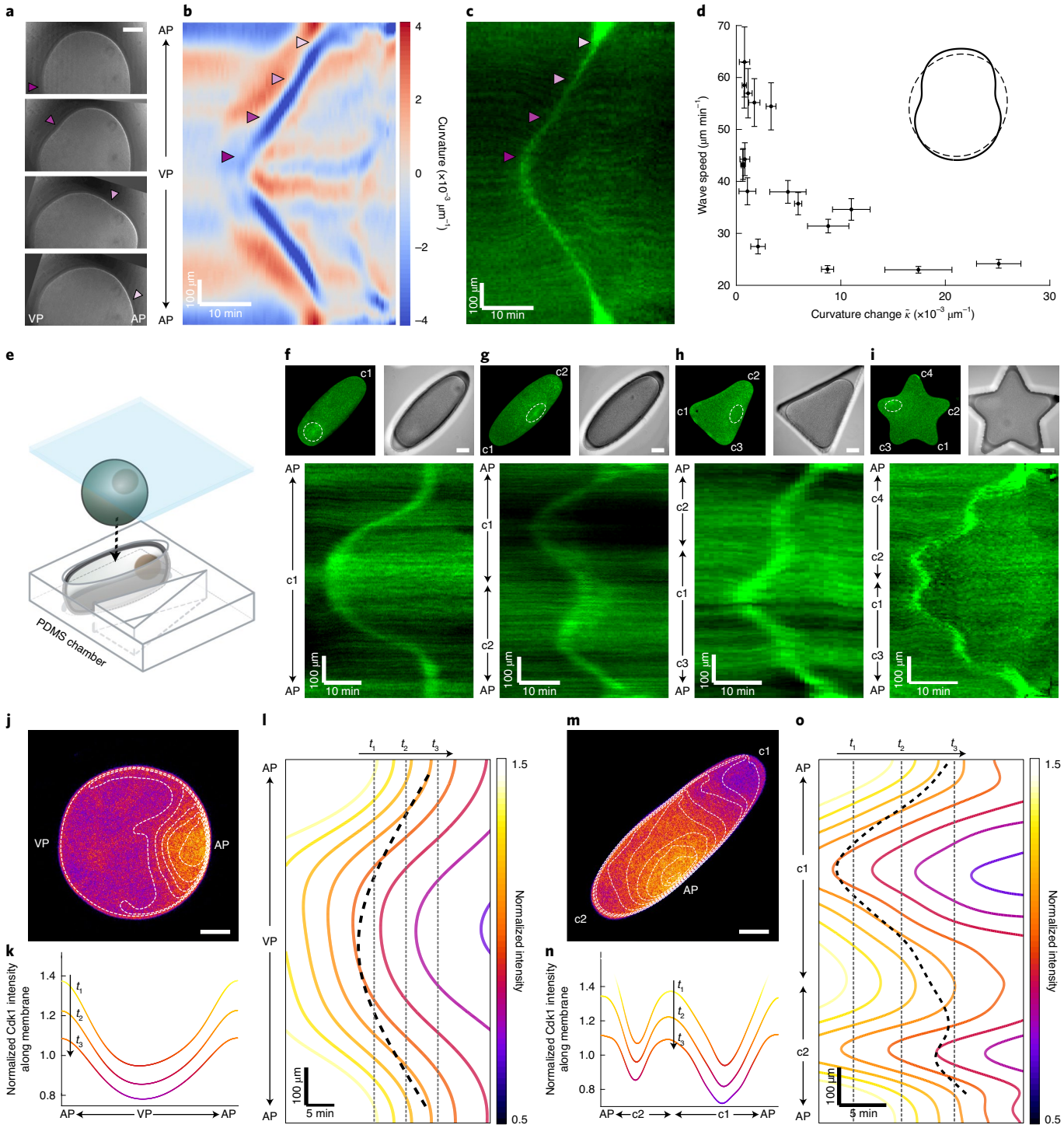


**Fig. 1 | Contraction waves in starfish oocytes confined in compartments with different geometries. a**, Differential interference contrast images of a surface contraction wave travelling from the VP to the AP during meiotic anaphase I. **b**, Kymograph of the surface contraction wave showing the trace of the cell surface curvature. **c**, Kymograph showing the distribution of active Rho-GTP (labelled with rGBD-GFP), which coincides with the surface contraction wave (Supplementary Video 1). **d**, Contraction wave speed plotted as a function of curvature change. Error bars indicate standard deviation (Methods). **e**, Schematic of the confinement experiments. PDMS, polydimethylsiloxane. **f**–**i**, Representative confocal cross-sections of Rho (top left), differential interference contrast images (top right) and membrane Rho kymographs of oocytes confined in different geometries: ellipse with AP at the tip ($N=4$) (**f**), ellipse with AP on the long side ($N=4$) (**g**), triangle ($N=6$) (**h**) and star ($N=2$) (**i**) (Supplementary Videos 2–5 and Supplementary Fig. 1). White dotted circles indicate positions of the nucleus. **j**–**o**, Spatiotemporal gradient of Cdk1-cyclinB in wild-type (circular) and elliptical oocytes. Confocal cross-sections of Cdk1-cyclinB distribution in wildtype oocyte (Supplementary Video 6, $N=3$) and in elliptical oocyte with AP on the long side (Supplementary Video 7, $N=2$) (**j**,**m**). Cdk1 distribution along the membrane at three different time points (**k**,**n**). The times $t_1$, $t_2$ and $t_3$ are 100 s, 400 s and 700 s, respectively, after the first wave initiation. Kymographs of the membrane Cdk1 gradient during passage of the surface contraction wave in wildtype and elliptical oocytes (**l**,**o**). The dotted line indicates the position of the Rho-GTP band estimated from cell surface deformation (Methods). Cdk1-cyclinB intensity is normalized to the value at the initiation point of the first wave. All white scale bars represent 50 μm.

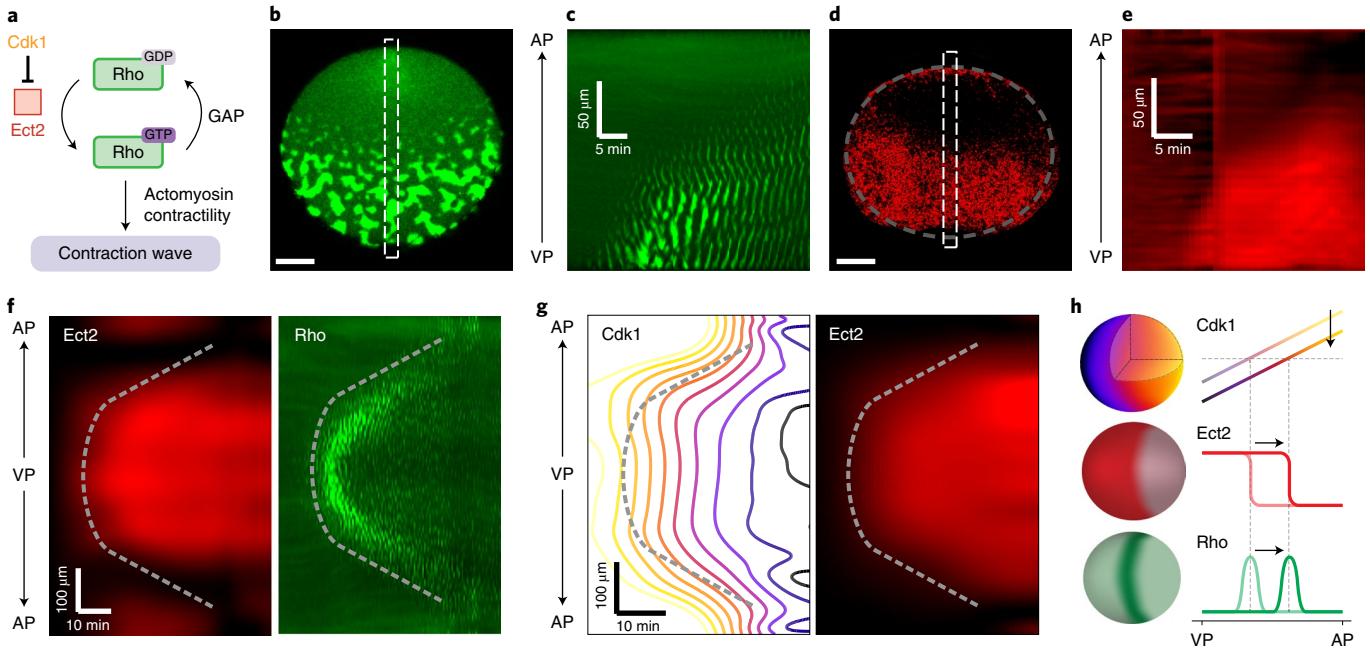


**Fig. 2 | The Cdk1–Ect2–Rho pattern hierarchy. a**, Biochemical interaction network of the signalling molecules that control surface contraction wave in starfish oocyte. GAP, GTPase-activating protein. **b**–**e**, Snapshots of the Rho spiral front (**b**) and the cumulative intensity difference of the Ect2 front (**d**) on the membrane during surface contraction wave propagation in an Ect2-overexpressing oocyte (Supplementary Videos 10 and 11). The kymographs show the Rho signal (**c**) and the cumulative intensity difference of Ect2 (**e**) within a narrow region around the AP–VP axis during surface contraction wave propagation (white dashed boxes in **b** and **d**, respectively). Grey dashed line in **d** marks the boundary of the cell. Scale bars in **b** and **d** represent 50 µm. **f**, Kymographs of Ect2 and Rho concentrations along the membrane of an oocyte expressing both rGBD-GFP and Ect2-mCherry during surface contraction wave propagation (Supplementary Video 12). **g**, Kymographs of Cdk1-cyclinB and Ect2 concentration along the membrane of an oocyte expressing both cyclinB-GFP (a marker for Cdk1 activity) and Ect2-mCherry during surface contraction wave (Supplementary Video 13). The Cdk1-cyclinB intensity is normalized as in Fig. 1l. Grey dotted lines in **f** and **g** are guides for the eyes showing approximately the front positions. **h**, Schematic showing how the spatial distributions of Cdk1-cyclinB (top), Ect2 (middle) and Rho (bottom) proteins couple to each other during surface contraction wave propagation.

show that, as the Cdk1 gradient decays, the Rho-GTP band (as indicated by the surface contraction wave) follows an isocline of the Cdk1-cyclinB concentration such that multiple waves arrive at the nucleus simultaneously. Hence, the Rho-GTP band on the membrane must follow a specific concentration of the decaying membrane Cdk1 gradient.

How can the Rho-GTP band be coupled to a particular level of Cdk1-cyclinB? A likely molecular link between the Cdk1 gradient and the Rho-GTP band is the Rho guanine nucleotide exchange factor (GEF) Ect2, which activates Rho (Fig. 2a). Cdk1-cyclinB phosphorylates Ect2, which has been suggested to decrease its membrane affinity[24]. Moreover, it has been reported that Ect2 overexpression induces a propagating front of Rho-GTP spiral waves (Rho spirals) instead of a Rho-GTP-band[25] (Fig. 2b,c and Supplementary Video 10). When we imaged the fluorescently tagged Ect2 (Methods), we observed that an Ect2 front coincides with the Rho-GTP band (Fig. 2d,e and Supplementary Video 11). We hypothesize that the Ect2 front follows a threshold of Cdk1-cyclinB concentration and that the Ect2 front in turn regulates the downstream Rho dynamics. To test these hypotheses, we simultaneously imaged Ect2 and Rho. Indeed, we find that the domain of high Ect2 concentration coincides with the domain of Rho spirals (Fig. 2f, dashed line, Supplementary Fig. 3a and Supplementary Video 12). Furthermore, simultaneous imaging of Ect2 and Cdk1-cyclinB confirmed that the Ect2 front approximately follows a single Cdk1-cyclinB level (Fig. 2g, dashed line, Supplementary Fig. 3b and Supplementary Video 13).

Taken together, these findings suggest that the propagating Rho-GTP band is a result of the following hierarchy of protein localization patterns (Fig. 2h). Cdk1-cyclinB forms a cytosolic gradient in the cell, which serves as a spatial map to guide a front of Ect2 by localizing the front interface to a threshold Cdk1-cyclinB level. The Ect2 front demarcates a domain of high Ect2 concentration and a domain of low Ect2 concentration, which provides a spatial cue for the Rho-GTP band on the membrane. This cue leads to a Rho-GTP band at the interface of the Ect2 front in the wild type, or Rho spirals in the high-concentration domain when Ect2 is overexpressed. As the position of the two Ect2 domains are determined by the Cdk1-cyclinB threshold concentration, the propagation of the Rho-GTP band is ultimately controlled by the degradation of Cdk1-cyclinB. To elucidate the underlying physical mechanism of this Cdk1–Ect2–Rho pattern hierarchy, we propose a reaction–diffusion model with two distinct modules. First, we demonstrate how the Ect2 front controls the downstream Rho-GTP band and spiral front dynamics. We then propose a mechanism for how the membrane Cdk1 gradient controls the position of the Ect2 front.

The first module of our model captures key features of the Rho GTPase cycle[26,27] (Fig. 3a and Supplementary Figs. 7 and 8). In its inactive GDP-bound state, Rho can either be membrane-bound or cytosolic (GDI-bound). Once bound to the membrane, Rho-GDP can undergo nucleotide exchange which converts it into an active GTP-bound state, a process mediated by GEFs. When Rho-GTP is hydrolysed by GTPase-activating proteins, it detaches from the membrane. The GEF Ect2 front demarcates subdomains on the membrane with high and low nucleotide exchange rates (Fig. 3a, Supplementary Figs. 11 and 13, and Supplementary Sections 2.3–2.6). Thus, viewed from a position on the membrane, the passing Ect2 front induces a sudden increase in the nucleotide exchange rates (Fig. 3b,c). Can such an increase lead to the observed Rho-GTP band? As the Ect2 increase shifts the steady-state concentration of Rho-GTP upwards, one might, at first glance, assume that this

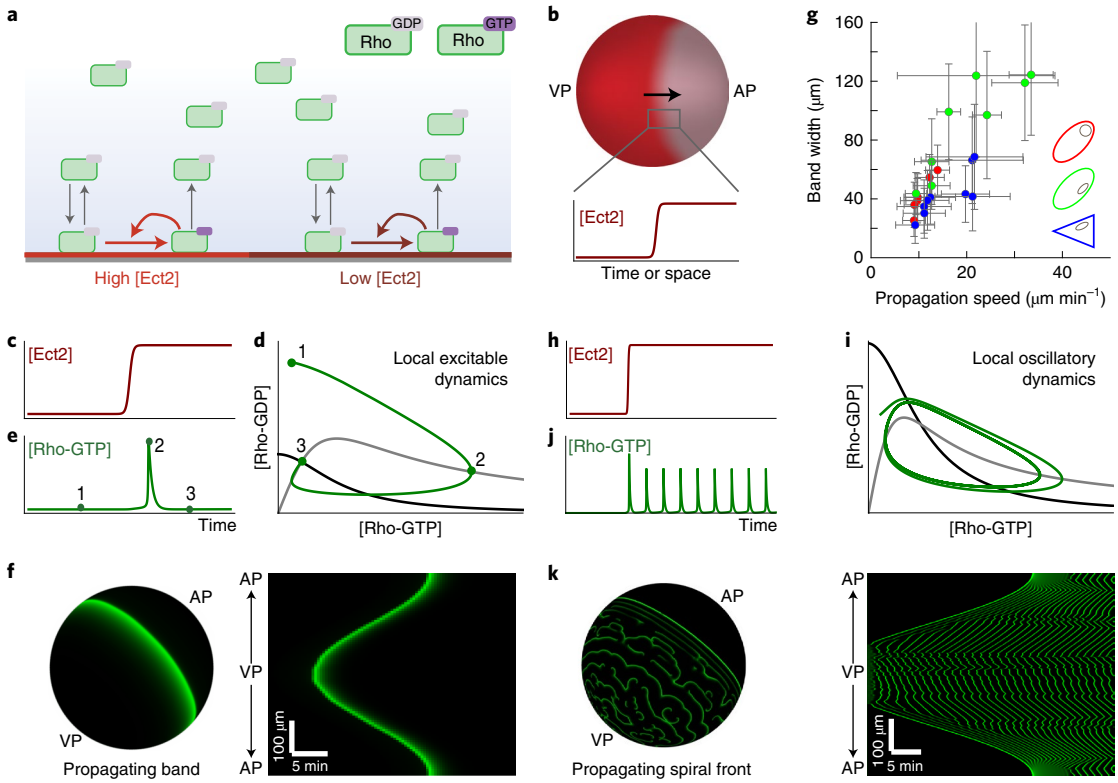


**Fig. 3 | Model of Rho dynamics. a**, Schematic of the reaction–diffusion dynamics of Rho proteins in different Ect2 subdomains. **b**, The Ect2 front, serving as an input to the model, effectively increases the nucleotide exchange rates, thereby activating Rho. Viewed from a single position on the membrane, the Ect2 concentration suddenly increases as the Ect2 front passes by. **c**–**e**, With local excitable dynamics, the sudden increase in Ect2 (**c**) leads to a large excursion of the dynamics in phase space (**d**, from point 1 to point 3) which results in a transient increase in the Rho-GTP concentration on the membrane (**e**, point 2). **f**, Snapshot of a finite element simulation of the Rho-GTP band travelling over the surface of a 3D sphere (Supplementary Video 14), with the accompanying kymograph of the travelling Rho-GTP band. **g**, Rho-GTP band width versus propagation speed in oocytes confined to three different geometries. The band width is calculated as the product of excitation time and propagation speed. Error bars indicate standard deviation. **h**–**j**, With local oscillatory dynamics, the increase in Ect2 (**h**) leads to oscillations along a limit cycle in phase space (**i**), which results in oscillatory Rho dynamics (**j**). **k**, Snapshot of a finite element simulation of the Rho spiral domain travelling over the surface of a 3D sphere (Supplementary Video 18), with the accompanying kymograph of Rho-GTP spirals. See Methods and Supplementary Tables 1 and 2 for the model equations and parameters used in **f** and **k**.

merely translates the Ect2 front into a Rho-GTP front. However, this focus on steady states assumes an instantaneous response and therefore overlooks the transient dynamics, which can be qualitatively different when the increase in the Ect2 concentration occurs suddenly (Supplementary Fig. 14). Consider an initially low Ect2 concentration, such that most Rho is in the inactive GDP-bound form (Fig. 3d,e, point 1). A sudden increase in the Ect2 concentration then shifts the steady state towards a (slightly) increased Rho-GTP and decreased Rho-GDP concentration on the membrane (Fig. 3d, points 1 to 3). Owing to the positive feedback on Rho activation, the Rho concentrations do not relax directly into the new steady state, but transition to it via a large excursion in phase space; in other words, the Rho dynamics are excitable (Supplementary Figs. 9 and 10, and Supplementary Sections 2.3 and 2.4). The large excursion in phase space corresponds to a transient increase in the Rho-GTP concentration on the membrane (Fig. 3d,e, point 2). Thus, the time differential of the local Ect2 concentration, rather than the absolute Ect2 level, induces the large transient increase in Rho activation.

As the Ect2 front moves along the membrane, it continuously triggers such local excitations, which results in a spatially localized band of Rho activity that follows the Ect2 front (Fig. 3f and Supplementary Video 14). Consequently, this model predicts that the width of the Rho-GTP band is given by the product of the excitation time and the propagation speed. We confirm this numerically using finite element simulations of the system in different geometries (Supplementary Videos 15–17). Indeed, we find that the band width is positively correlated with the propagation speed (Supplementary Fig. 15). To test this prediction experimentally, we confine oocytes in three different geometries and also observe the predicted increase in band width with propagation speed (Fig. 3g).

In oocytes that overexpress Ect2, we observe a propagating front of Rho-GTP spirals (Fig. 2c). Viewed from a fixed position on the membrane, spirals correspond to oscillations in Rho-GTP concentration. In accordance with this experimental observation, our model exhibits limit-cycle oscillations over a broad parameter regime (Fig. 3h,i, Supplementary Fig. 12 and Supplementary Sections 2.4 and 2.7). Indeed, our simulations show that the resulting oscillatory medium can exhibit spiral waves (Fig. 3k, Supplementary Fig. 16 and Supplementary Video 18). In fact, this is generic because excitability and limit-cycle oscillations are closely related nonlinear phenomena, and are often found in neighbouring parameter regimes. The model provides a mechanism that explains how different levels of Ect2 can account for both the Rho-GTP band and spiral wave dynamics in the starfish oocyte. In addition, it shows that the propagation of the Ect2 front fully determines the propagation of the Rho-GTP band, and therefore the surface contraction wave.

To elucidate how the propagating Rho-GTP band adapts to changes in cell shape, we ask how the propagating Ect2 front itself is

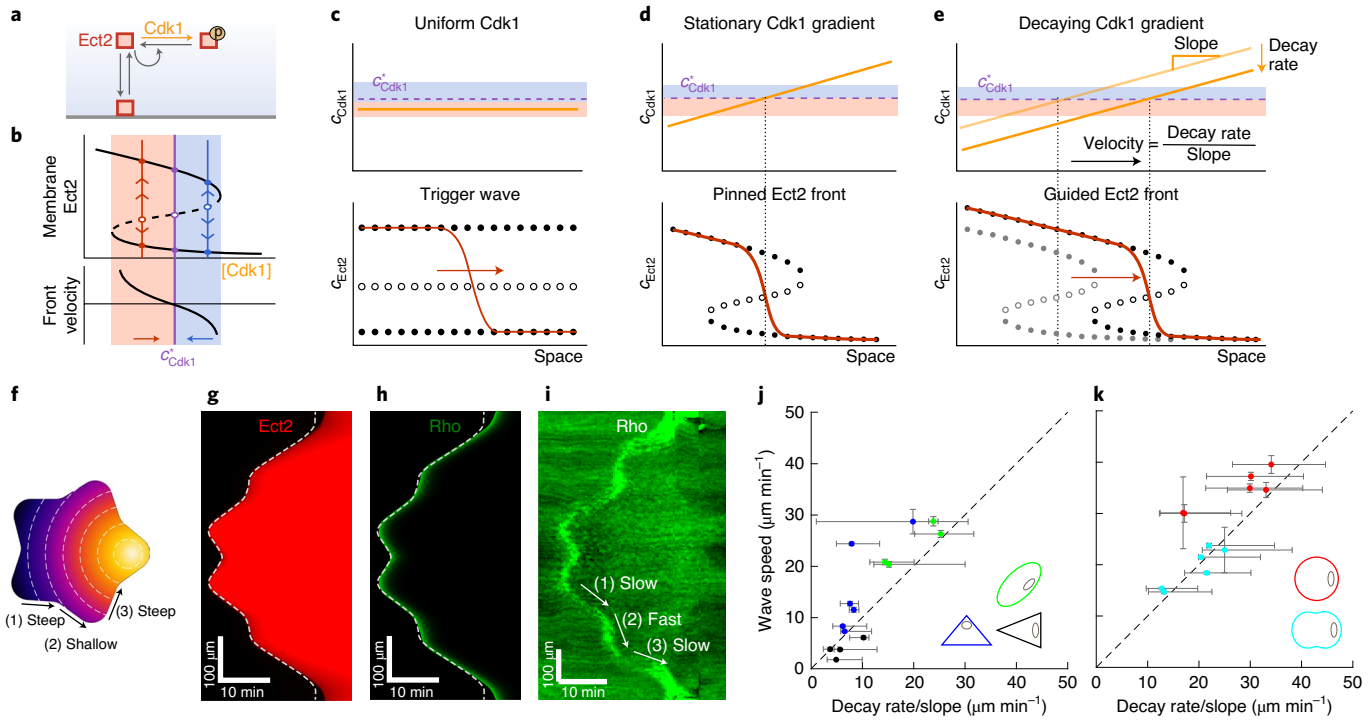


**Fig. 4 | Model of Ect2 front regulation by the Cdk1-cyclinB gradient. a**, Schematic of the reaction–diffusion dynamics of Ect2. **b**, Schematic representation of the bistable regime of membrane-bound Ect2 when the Cdk1-cyclinB dependent phosphorylation rate is varied. **c**, A uniform Cdk1-cyclinB distribution induces an Ect2 trigger wave. **d**, A stationary Cdk1 gradient pins an Ect2 front at the $c^*_{Cdk1}$ threshold level. **e**, A decaying Cdk1 gradient guides the propagation of the Ect2 front pinned at the $c^*_{Cdk1}$ threshold level. The blue and orange regions in **b**–**e** mark the Cdk1 concentration for which, respectively, the high and low steady states are dominant. The solid and open circles in **c**–**e** represent stable and unstable steady states, respectively. The yellow lines represent the Cdk1 concentration and the red lines represent the Ect2 concentration. **f**, Snapshot of the Cdk1 gradient in the star geometry. **g**,**h**, Kymographs of simulated Ect2 front (**g**) and Rho band (**h**) in the star geometry (Supplementary Video 17). The grey dotted line shows an isocline of the membrane Cdk1 gradient. The model equations are defined in the Methods, and parameters are as in Supplementary Tables 1 and 2 (see also Supplementary Sections 2.2 and 3.2). **i**, Experimental kymograph of Rho-GTP band propagation in a star-shaped oocyte correlates with that of the Cdk1 gradient along the membrane. **j**,**k**, The Rho-GTP band speed in different static (**j**) and dynamic (**k**) geometries plotted against the quotient of decay rate and slope of the Cdk1 gradient. Error bars indicate maximum and minimum values measured at the start and end of each segment (Methods).

controlled by the upstream Cdk1 gradient. Propagating fronts are a generic feature of bistable media. These fronts connect two plateaus, which correspond to the two stable steady states[28,29], and propagate such that the steady state with the stronger attraction (dominant steady state) invades the other steady state. Although such a mechanism of front propagation does not depend on the precise origin of the underlying bistability, we hypothesize that a candidate for bistable dynamics in starfish oocytes is Ect2, potentially as part of an interaction network with other Rho regulators, in which active (unphosphorylated) Ect2 autocatalytically enhances its own dephosphorylation (Fig. 4a, Supplementary Fig. 18 and Supplementary Section 3.2). Furthermore, we assume that Ect2 can be phosphorylated by cytosolic Cdk1-cyclinB[24] and that Ect2 can only bind to or detach from the membrane in its active conformation. These reaction kinetics exhibit bistability for a range of Cdk1-cyclinB concentrations, with the two steady states corresponding to high and low Ect2 concentrations on the membrane (Fig. 4b and Supplementary Fig. 15). To demonstrate the bistable nature of Ect2 dynamics, we developed a photo-recruitable GEF catalytic domain in starfish oocytes[30] (Methods). We showed that oocyte contractility exhibits an abrupt and switch-like response to membrane GEF recruitment (Supplementary Fig. 4 and Supplementary Video 19). This result, together with the observation that Ect2 forms a front, suggests that Ect2 activation dynamics are bistable.

In the model, the Cdk1-cyclinB concentration determines the relative dominance between the two steady states, and therefore the speed of the Ect2 front (Fig. 4c). For a critical Cdk1-cyclinB concentration, $c^*_{Cdk1}$ (Fig. 4b, purple line, and Supplementary Fig. 19), the front is equally attracted to both steady states, which results in a stalled front. As Cdk1-cyclinB forms a gradient, the critical concentration $c^*_{Cdk1}$ at which the front stalls corresponds to a certain position on the membrane, and the Ect2 front will move towards this position, where it in turn stalls[31] (Fig. 4d). As the gradient decays, this stalling point will itself move in space, which causes the Ect2 front to follow (Fig. 4e and Supplementary Fig. 20). Hence, the speed at which the stalling point moves along the membrane is determined by the ratio of the decay rate (temporal variation of the concentration) to the slope (spatial variation of the concentration) of the Cdk1 gradient (Fig. 4e). This implies that the speed of the Ect2 front, and therefore of the Rho-GTP band, is determined by the same ratio. By simulating the reaction–diffusion dynamics numerically, we indeed find that the Ect2 front propagates up to the stalling point and then follows this concentration as the gradient decays (Supplementary Videos 15–17). Thus, propagation of the Ect2 front is strongly correlated with, and limited by, the speed of the stalling point.

We have identified a direct link between the speed of the Rho-GTP band and the decaying Cdk1 gradient. Based on this insight, we can now explain how the propagating Rho-GTP band adapts to the cell shape. A striking example that illustrates this adaptation is the propagation of the Rho-GTP band in a star geometry, in which the different arms of the star exhibit membrane Cdk1 gradients of varying slope (Fig. 4f). As a consequence, the speed of the Ect2 front

and the Rho-GTP band vary greatly from slow speed along arms with steep gradients to high speed along arms with shallow gradients. We verified this using finite element simulation (Fig. 4g,h), which agrees well with the experimental data (Fig. 4i). To further test this relationship between the speed of the Rho-GTP band and the decaying gradient quantitatively, we analysed the Cdk1-cyclinB distribution in different cell shapes and measured both the average slope and average decay rate of the membrane Cdk1 gradient (Supplementary Section 1.2). We estimated the front speed from the membrane deformation induced by the surface contraction wave (Supplementary Section 1.2 and Supplementary Fig. 5). By combining measurements of multiple surface contraction waves from different cell shapes, we indeed find that the propagation speed is positively correlated with, and limited by, the ratio of the decay rate to the slope of the membrane Cdk1 gradient (Fig. 4j).

As a final test of our model, we ask whether the Cdk1–Ect2–Rho pattern hierarchy can explain the negative correlation between the speed of the Rho-GTP band and the magnitude of deformation during the contraction wave (Fig. 1d). We reason that the contraction wave must reorient the membrane with respect to the gradient, such that the Cdk1 gradient along the membrane becomes steeper, resulting in a slower front propagation. In agreement with this expectation, we find that for oocytes with a larger shape deformation, the ratio of the decay rate to the slope of Cdk1 gradient is reduced (Fig. 4k). Furthermore, our proposed mechanism predicts that the Cdk1 gradient during meiosis II should be shallower or should decay faster, resulting in a faster progression of the surface contraction wave during meiotic anaphase II (Supplementary Fig. 6).

The shape-adaptation mechanism confers robustness to cell shape changes by integrating positional information encoded in the Cdk1 gradient with self-organized protein patterns[32] of Ect2 and Rho. The excitable dynamics underlying the Rho-GTP band are reminiscent of the spiking dynamics in neural systems[33], which suggests that information processing on widely differing scales arises from similar organizing principles. The hierarchical coupling of bistability and excitability elucidates how the Rho-GTP band and spiral front propagation arise from the same underlying regulatory network and unify the two phenomena that have been previously reported separately[21,25,34]. In addition, the Cdk1–Ect2–Rho hierarchy processes cell shape information to induce a mechanochemical response. As Rho induces actomyosin contractility to change cell shape, this mechanism provides a mechanochemical feedback loop that could also facilitate cell shape control, a process that is distinct from previously reported mechanochemical coupling mechanisms[35,36]. Although the shape-adaptation mechanism reported here is solely based on the Cdk1 gradient, there could also be subtle effects from cell mechanics. In future work, it would be instructive to explore the interplay of cortical tension with cell shape and biochemical dynamics in the context of putative mechanochemical feedbacks[35,36]. Interestingly, the Cdk1–Ect2–Rho hierarchy shows striking similarities with surface contraction waves in *Xenopus* eggs[37], nuclear positioning[38] and cell cycle waves in *Drosophila* embryos[39,40], and with morphogenetic furrow formation during *Drosophila* eye development[41], which suggests that our results may underpin a wide range of cellular patterning processes. We hypothesize that this hierarchical coupling of protein patterns is a generic mechanism that facilitates robust spatiotemporal information processing on various scales, from single cells to tissues.

## Online content

Any methods, additional references, Nature Research reporting summaries, source data, extended data, supplementary information, acknowledgements, peer review information; details of author contributions and competing interests; and statements of data and code availability are available at https://doi.org/10.1038/s41567-021-01164-9.

Received: 5 February 2020; Accepted: 8 January 2021;
Published online: 15 February 2021

## References

1. Théry, M. & Bornens, M. Cell shape and cell division. *Curr. Opin. Cell Biol.* **18**, 648–657 (2006).
2. Minc, N., Burgess, D. & Chang, F. Influence of cell geometry on division-plane positioning. *Cell* **144**, 414–426 (2011).
3. Gray, A. N. et al. Coordination of peptidoglycan synthesis and outer membrane constriction during *Escherichia coli* cell division. *Elife* **4**, e07118 (2015).
4. Mogilner, A. & Keren, K. The shape of motile cells. *Curr. Biol.* **19**, R762–R771 (2009).
5. Razzell, W., Wood, W. & Martin, P. Recapitulation of morphogenetic cell shape changes enables wound re-epithelialisation. *Development* **141**, 1814–1820 (2014).
6. Heisenberg, C.-P. & Bellaïche, Y. Forces in tissue morphogenesis and patterning. *Cell* **153**, 948–962 (2013).
7. Martin, A. C. & Goldstein, B. Apical constriction: Themes and variations on a cellular mechanism driving morphogenesis. *Development* **141**, 1987–1998 (2014).
8. Halatek, J., Brauns, F. & Frey, E. Self-organization principles of intracellular pattern formation. *Phil. Trans. R. Soc. B* **373**, 20170107 (2018).
9. Antonny, B. Mechanisms of membrane curvature sensing. *Annu. Rev. Biochem.* **80**, 101–123 (2011).
10. Wu, Z., Su, M., Tong, C., Wu, M. & Liu, J. Membrane shape-mediated wave propagation of cortical protein dynamics. *Nat. Commun.* **9**, 136 (2018).
11. Liu, A. P. et al. Membrane-induced bundling of actin filaments. *Nat. Phys.* **4**, 789–793 (2008).
12. Thalmeier, D., Halatek, J. & Frey, E. Geometry-induced protein pattern formation. *Proc. Natl Acad. Sci. USA* **113**, 548–553 (2016).
13. Rangamani, P. et al. Decoding information in cell shape. *Cell* **154**, 1356–1369 (2013).
14. Harvey, E. N. & Fankhauser, G. The tension at the surface of the eggs of the salamander, Triturus (Diemyctylus) viridescens. *J. Cell. Comp. Physiol.* **3**, 463–475 (1933).
15. Kojima, M. K. Cyclic changes of the cortex and the cytoplasm of the fertilized and the activated sea urchin egg. *Embryologia* **7**, 81–94 (1962).
16. Hara, K., Tydeman, P. & Kirschner, M. A cytoplasmic clock with the same period as the division cycle in *Xenopus* eggs. *Proc. Natl Acad. Sci. USA* **77**, 462–466 (1980).
17. Sawai, T. Wavelike propagation of stretching and shrinkage in the surface of the newt's egg before the first cleavage. *J. Exp. Zool.* **222**, 59–68 (1982).
18. Houliston, E., Carré, D., Johnston, J. A. & Sardet, C. Axis establishment and microtubule-mediated waves prior to first cleavage in *Beroe* ovata. *Development* **117**, 75–87 (1993).
19. Quaas, J. & Wylie, C. Surface contraction waves (SCWs) in the *Xenopus* egg are required for the localization of the germ plasm and are dependent upon maternal stores of the kinesin-like protein Xklp1. *Dev. Biol.* **243**, 272–280 (2002).
20. Klughammer, N. et al. Cytoplasmic flows in starfish oocytes are fully determined by cortical contractions. *PLoS Comput. Biol.* **14**, e1006588 (2018).
21. Bischof, J. et al. A cdk1 gradient guides surface contraction waves in oocytes. *Nat. Commun.* **8**, 849 (2017).
22. Bischof, J. *The Molecular Mechanism of Surface Contraction Waves in the Starfish Oocyte*. PhD thesis, Univ. Heidelberg (2016).
23. Wolpert, L. Positional information and pattern formation. *Curr. Top. Dev. Biol.* **117**, 597–608 (2016).
24. Su, K.-C., Takaki, T. & Petronczki, M. Targeting of the RhoGEF Ect2 to the equatorial membrane controls cleavage furrow formation during cytokinesis. *Dev. Cell* **21**, 1104–1115 (2011).
25. Bement, W. M. et al. Activator–inhibitor coupling between Rho signalling and actin assembly makes the cell cortex an excitable medium. *Nat. Cell Biol.* **17**, 1471–1483 (2015).
26. Hodge, R. G. & Ridley, A. J. Regulating Rho GTPases and their regulators. *Nat. Rev. Mol. Cell Biol.* **17**, 496–510 (2016).
27. Müller, P. M. et al. Systems analysis of RhoGEF and RhoGAP regulatory proteins reveals spatially organized RAC1 signalling from integrin adhesions. *Nat. Cell Biol.* **22**, 498–511 (2020).
28. Mikhailov, A. S. *Foundations of Synergetics I: Distributed Active Systems* 2nd edn (Springer Science & Business Media, 2012).
29. Gelens, L., Anderson, G. A. & Ferrell, J. E. Spatial trigger waves: positive feedback gets you a long way. *Mol. Biol. Cell* **25**, 3486–3493 (2014).
30. Wagner, E. & Glotzer, M. Local RhoA activation induces cytokinetic furrows independent of spindle position and cell cycle stage. *J. Cell Biol.* **213**, 641–649 (2016).
31. Rulands, S., Klünder, B. & Frey, E. Stability of localized wave fronts in bistable systems. *Phys. Rev. Lett.* **110**, 038102 (2013).

32. Green, J. B. A. & Sharpe, J. Positional information and reaction–diffusion: two big ideas in developmental biology combine. *Development* **142**, 1203–1211 (2015).
33. Izhikevich, E. M. *Dynamical Systems in Neuroscience: The Geometry of Excitability and Bursting* (MIT Press, 2010).
34. Tan, T. H. et al. Topological turbulence in the membrane of a living cell. *Nat. Phys.* **16**, 657–662 (2020).
35. Howard, J., Grill, S. W. & Bois, J. S. Turing's next steps: The mechanochemical basis of morphogenesis. *Nat. Rev. Mol. Cell Biol.* **12**, 392–398 (2011).
36. Gross, P., Kumar, K. V. & Grill, S. W. How active mechanics and regulatory biochemistry combine to form patterns in development. *Annu. Rev. Biophys.* **46**, 337–356 (2017).
37. Chang, J. B. & Ferrell, J. E.Jr. Mitotic trigger waves and the spatial coordination of the *Xenopus* cell cycle. *Nature* **500**, 603–607 (2013).
38. Deneke, V. E. et al. Self-organized nuclear positioning synchronizes the cell cycle in *Drosophila* embryos. *Cell* **177**, 925–941.e17 (2019).
39. Vergassola, M., Deneke, V. E. & Di Talia, S. Mitotic waves in the early embryogenesis of *Drosophila*: bistability traded for speed. *Proc. Natl Acad. Sci. USA* **115**, E2165–E2174 (2018).
40. Deneke, V. E., Melbinger, A., Vergassola, M. & Di Talia, S. Waves of Cdk1 activity in S phase synchronize the cell cycle in *Drosophila* embryos. *Dev. Cell* **38**, 399–412 (2016).
41. Curtiss, J. & Mlodzik, M. Morphogenetic furrow initiation and progression during eye development in *Drosophila*: the roles of decapentaplegic, hedgehog and eyes absent. *Development* **127**, 1325–1336 (2000).

## Methods

**Experimental methods.** *Starfish oocyte preparation.* Starfish *Patiria Miniata* was procured from South Coast Bio-Marine. The animals were kept in a salt-water fish tank maintained at 15 °C. The ovaries were extracted through a small incision made at the bottom of the starfish. The ovaries were carefully fragmented using a pair of scissors to release the oocytes. Extracted oocytes were washed twice with calcium-free seawater to prevent maturation and were incubated in filtered seawater at 15 °C. Experiments were performed within three days of oocyte extraction. To induce large shape deformation, oocytes are incubated in 0.1 mg mL$^{-1}$ actinase E for 30 min.

*Constructs.* The following constructs used were described in previous studies: GFP-labelled rhotekin-binding domain construct EGFP-rGBD[42] (Addgene plasmid #26732); 3XmCherry-labelled Ect2[43] (gift from K.-C. Su); and EGFP-labelled cyclinB[21] (gift from P. Lenart). In addition, the constitutively active Ect2 construct fluorescently labelled with mCherry, mCherry-Ect2-T808A, was used (gift from G. von Dassow).

To manipulate Rho activity with light, we adapted the TULIP optogenetic system[30] to enable photo-recruitment of GEF to the membrane. The system consists of two components: a membrane-targeted photosensitive domain LOVpep, and a GEF LARG fused with tandem PDZ tag that binds to LOVpep in a 405 nm light-dependent manner. To adapt this system in starfish oocyte, we cloned the Stargazin-GFP-LOVpep (Addgene plasmid #80406, using primers atggggctgtttgatcgagg and ttacacccaggtatccaccgc) and PR-GEF YFP (2XPDZ-YFP-LARG DH, Addgene plasmid #80408, using primers atggcaaaacaagagattcgagtga and ttagcgctgcttgttttctgcc) into pCS2+8 backbone constructs[44] (Addgene plasmid #34931). Stargazin-GFP-LOVpep and PR-GEF YFP (2XPDZ-YFP-LARG DH) were gifts from M. Glotzer and PCS2+8 was a gift from A. Hamdoun.

*In vitro synthesis of mRNA and microinjection.* For in vitro synthesis of mRNA, we first amplified the constructs by bacterial growth overnight. The plasmids were then purified using Miniprep (Qiagen) and linearized using the appropriate restriction enzymes. EGFP-rGBD and 3XmCherry-Ect2 mRNA were synthesized using the SP6 mMessage mMachine transcription kits (Thermo Fisher Scientific). CyclinB-EGFP mRNA was synthesized using the T7 Ultra mMessage mMachine transcription kits (Thermo Fisher Scientific). To express the constructs, the synthesized mRNA was microinjected into the cytoplasm of the oocytes and incubated overnight at 15 °C.

*Chamber fabrication.* Microfabricated chambers were fabricated by casting polydimethylsiloxane (PDMS) onto patterned silicon wafers. The chamber shapes were designed with a height of 80 μm and surface area of around 27,000 μm$^2$, to match typical volumes of the oocytes. The patterned silicon wafer was manufactured using photolithography (Microfactory SAS). The silicon wafer was silanized with trichlorosilane (Sigma, product number 448931). PDMS was made by mixing Dow SYLGARD 184 Silicone Elastomer Clear solution at a 10:1 ratio of base to curing agent. After thorough mixing, the elastomer was poured over the silicon master mold, degassed in a vacuum chamber and cured at 60 °C in an oven for 1 h.

*Confocal imaging.* Fluorescence imaging was performed on either the Zeiss 700 or 710 laser scanning confocal microscope (LSM) system. The Zeiss 700 laser scanning confocal system consists of a Zeiss AxioObserver motorized inverted microscope stand, an LSM photomultiplier detector and a transmitted light detector. Images were acquired using a ×40/NA = 1.3 Oil Plan-Apochromat objective with the appropriate laser line and emission filter. The system was operated using Zeiss Zen 2010 acquisition software.

The Zeiss 710 laser scanning confocal system consists of a Zeiss AxioObserver motorized inverted microscope stand with differential interference contrast optics, motorized XY stage, two LSM photomutiplier detectors and a transmitted light detector. Images were acquired using a ×40/NA = 1.1 Water LD C-Apochromat objective with the appropriate laser line and emission filter. The system was operated using Zeiss Zen Black 2012 acquisition software.

**Image analysis and quantification.** *Space–time kymograph of Rho-GTP.* The space–time kymograph of GFP-labelled Rho-GTP $I_R(s, t)$ is computed by first extracting the boundary of the oocyte $\mathbf{r}(s) = (x(s), y(s))$ and then extracting the fluorescence intensity $I_R(s)$ along the boundary for all time frames $t$. Here, we used $s$ to parameterize the arc length of the oocyte boundary. For each time frame $t$, we performed a Gaussian filtering step (with a standard deviation of 1.2 pixels) on the confocal image of the oocyte cross-section before applying a thresholding step (with threshold level set at 80% of the mean intensity of each frame) to make a binary image. The oocyte boundary $\mathbf{r}(s)$ is obtained by using the 'bwboundaries' function in MATLAB on the binary image, which is then smoothed using the MATLAB function 'smoothing'. The intensity $I_R(s)$ is obtained by first identifying a local window with a size of 12×12 pixels that is centred at $\mathbf{r}(s)$, and then taking the mean intensity of the pixels in the top 50th percentile intensity within the local window. To construct the full kymograph $I_R(s, t)$, the intensity $I_R(s)$ at each time frame $t$ is aligned such that the AP corresponds to the same arc length position and is resampled at the appropriate arc length $s$.

*Space–time kymograph of membrane curvature change.* From the oocyte boundaries $\mathbf{r}(s) = (x(s), y(s))$ measured for all time points, the positions $x(s)$ and $y(s)$ are aligned to a common point (consistent with the alignment for $I_R(s)$) and are resampled at the appropriate arc length $s$ to produce $\tilde{x}(s)$ and $\tilde{y}(s)$. The in-plane membrane curvature is computed using the resampled positions and according to the equation

$$\kappa = \frac{|\tilde{x}'\tilde{y}'' - \tilde{y}'\tilde{x}''|}{(\tilde{x}'^2 + \tilde{y}'^2)^{3/2}}$$

where primes refer to the derivative with respect to arc length $s$. The full curvature kymograph $\kappa(s, t)$ is obtained by repeating the calculation for all time points $t$. The kymograph of membrane curvature change $\tilde{\kappa}(s, t)$ is obtained by subtracting the rest state curvature $\kappa(s, t=0)$ from the kymograph. The contraction wave appears as a band of negative values in the curvature change kymograph. The maximum curvature change plotted in Fig. 1d is the average of six curvature values that are sampled mid-wave (when the curvature change is at a maximum). The error bar is the standard deviation of the six values. To minimize batch-to-batch variation, all experiments in Fig. 1d are performed using oocytes from the same batch.

*Space–time kymograph and contour plot Cdk1.* The Cdk1 concentration near the membrane $c(s)$ is obtained by averaging the intensity measurements within an annulus region beneath the membrane. A set of four progressively smaller perimeters that share the same centroid are obtained from the oocyte boundary $\mathbf{r}(s) = (x(s), y(s))$ with dilation factors (0.95, 0.91, 0.87 and 0.83). The intensity $I_{C_i}(s)$ along the $i$th perimeter $\mathbf{r}_i(s)$ is obtained by first identifying a local window with a size of 12×12 pixels that is centred at $\mathbf{r}_i(s)$, and then taking the mean intensity of the pixels in the top 50th percentile intensity within the local window. The fluorescence intensity of Cdk1 $I_C(s)$ is obtained by taking the average of the four intensities $I_{C_i}(s)$. To construct the full kymograph $I_C(s, t)$, the fluorescence intensity $I_C(s)$ at each time frame $t$ is aligned such that the AP corresponds to the same arc length position and is resampled at the appropriate arc length $s$. The final kymograph is obtained by normalizing $I_C(s, t)$ with the concentration of Cdk1 at the point at which the contraction wave was first initiated, $c_0$. The contour plot is obtained from the kymograph using MATLAB function 'contour'. Supplementary Fig. 2 shows confocal cross-sections and the corresponding kymographs for a freely floating oocyte and oocytes confined to elliptical and triangular geometries.

*Space–time kymograph of Ect2.* The Ect2 kymograph along the cell boundary $I_E(s, t)$ is obtained using a method similar to that for the Cdk1 kymograph, with one notable difference. In addition to background fluorescence from cytosolic Ect2-mCherry, the cortex of starfish oocyte contains granules with autofluorescence in the mCherry fluorescence window. To better separate signal from background, the fluorescence intensity of Ect2 $I_E(s)$ at each time point is first obtained from the oocyte boundary $\mathbf{r}(s)$ using the same approach as for the Cdk1 intensity $I_C(s)$, but with three dilation factors (0.95, 0.91 and 0.87) instead of four. To remove noise, a smoothing spline is fitted to $I_E(s)$ using the MATLAB smoothing spline function 'spaps', with the tolerance value set at 10% of the range of $I_E(s)$ (that is, tol = $[\max I_E(s) - \min I_E(s)]/10$). To remove background, the time difference of $I_E(s)$ at subsequent time point $\Delta I_E(s, t) = I_E(s, t) - I_E(s, t-1)$ is obtained. The final Ect2 kymograph, $I_E(s, t)$, is taken to be the cumulative sum of the intensity difference $\Delta I_E(s, t)$, that is, $I_E(s, t) = \sum_{\tau=1}^{t} \Delta I_E(s, \tau)$.

The Ect2 cumulative difference snapshot and kymograph in Fig. 2b is obtained using a similar procedure for background subtraction. Starting from the raw video for $I_E(\mathbf{r}, t)$ (Supplementary Video 10, left), we computed the temporal intensity difference at subsequent time point $\Delta I_E(\mathbf{r}, t) = I_E(\mathbf{r}, t) - I_E(\mathbf{r}, t-1)$. The final cumulative difference snapshot is taken to be $I_E(\mathbf{r}, t) = \sum_{\tau=1}^{t} \Delta I_E(\mathbf{r}, \tau)$ (Supplementary Video 10, right). The kymograph in Fig. 2b is obtained by taking the average intensity of a thin section in the middle of membrane over the duration of the surface contraction wave.

*Co-localization of Ect2 with Cdk1/Rho-GTP.* To show that the Ect2 front co-localizes with Cdk1/Rho-GTP, we co-expressed Ect2-mCherry with cyclinB-GFP/rGBD-GFP (Rho-GTP reporter) simultaneously and performed confocal imaging. We extracted the space–time kymograph of Ect2 together with Cdk1/Rho-GTP as described above. We were unable to visualize co-localization of Ect2 with Rho pulse for the wildtype condition, as we lack the tools to label the endogenous pool of Ect2 proteins. However, our Ect2/Rho-GTP two-colour imaging experiment clearly demonstrates that the Ect2 front co-localizes well with a Rho-GTP spiral front.

*Cdk1 decay rate γ and slope α calculation.* To estimate the decay rate $\gamma$, the total Cdk1 intensity over the entire oocyte boundary, $I_{C_T}(t) = \sum_s I_C(t, s)$, is plotted as a function of time. The intensity curve is approximately linear over the time window of the wave. The decay rate $\gamma$ is obtained by taking the slope of the linear line connecting $I_{C_T}(t_{start})$ and $I_{C_T}(t_{end})$. The spatial slope of Cdk1 can be estimated

from the spatial profile of Cdk1 at mid-wave, $I_{C_{mid}}(s) = I_C(s, t_{mid})$. The slope $\alpha$ for each wave segment is obtained by taking the slope of the linear line connecting $I_{C_{mid}}(s_{start})$ and $I_{C_{mid}}(s_{end})$, where $s_{start}$ and $s_{end}$ are the initiation and the annihilation position of each wave segment. The slopes similarly calculated from the spatial profiles of Cdk1 at the start and end of the wave $I_C(s, t_{start})$ and $I_C(s, t_{end})$ are used as upper and lower error bars.

*Ect2 front speed calculation from oocyte shape deformation.* As the membrane deformation arises from the Rho peak, which in turn localizes at the Ect2 front, we use the deformation of the membrane as a proxy for the Ect2 front position. To estimate the Ect2 front speed, we track the point of maximal deformation of the membrane along the arc length. From the curvature kymograph $\kappa(s, t)$, the curvature difference $\Delta\kappa(s, t) = \kappa(s, t) - \kappa(s, t-1)$ is computed. For a particular arc length location $s$, we found that the point at which curvature change $\Delta\kappa(t)$ passes zero is a good estimate of the Rho peak position. We verified this by performing Rho fluorescent imaging and showed that the Rho peak trajectory corresponds to point of maximal deformation identified from $\Delta\kappa(s, t)$ (Supplementary Fig. 5). After identifying all the points of zero crossing in the curvature difference kymograph $\Delta\kappa(s, t)$, a straight line is fitted for each wave segment. The slope of the linear line gives the Ect2 front speed for the particular oocyte segment. The error bar is the 95% prediction interval.

**Reaction–diffusion model for Rho and Ect2 module.** In this section, we specify the model equations and parameters. For a detailed description of the model, we refer to Supplementary Sections 2 and 3.

*Reaction–diffusion equations for the Ect2 module.* We propose a model in which Ect2 cycles between an inactive phosphorylated state (concentration $u_{Ep}(\mathbf{r}, t)$) and an active non-phosphorylated state (concentration $u_E(\mathbf{r}, t)$). Furthermore, we assume that active Ect2 can bind to and detach from the membrane ($u_e(\mathbf{r}, t)$). Ect2 can diffuse on the surface of a two-dimensional elliptical, triangular or star geometry, which represents the focus plane in experiments of geometrically confined oocytes. To describe the dynamics of Ect2, we use a reaction–diffusion model:

$$\begin{aligned}\partial_t u_E &= D_c\nabla^2 u_E + f_E(u_E, u_{Ep}, u_e)\\ \partial_t u_{Ep} &= D_c\nabla^2 u_{Ep} + f_{Ep}(u_E, u_{Ep}, u_e)\\ \partial_t u_e &= D_m\nabla^2 u_e + f_e(u_E, u_{Ep}, u_e),\end{aligned}$$

where $D_c$ and $D_m$ are the diffusion constant of the cytosolic components and membrane component, respectively. Motivated by the observation that Ect2 forms a front pattern on the membrane (Fig. 2d), we propose a model that exhibits bistability with the following reaction kinetics:

$$\begin{aligned}f_E &= k_{off}u_e - k_{on}u_E - \frac{k_{[Cdk1]}u_E}{K_p+u_E} + (k_{dp} + k_{fb}u_E)u_{Ep},\\ f_{Ep} &= \frac{k_{[Cdk1]}u_E}{K_p+u_E} - (k_{dp} + k_{fb}u_E)u_{Ep},\\ f_e &= k_{on}u_E - k_{off}u_e.\end{aligned}$$

These reaction kinetics conserve total protein mass, such that $\int_\Omega d\mathbf{r}(u_E + u_{Ep} + u_e) = n_E$ (where $\Omega$ denotes the computational domain) remains constant. The active Ect2 conformation can attach to and detach from the membrane with the rates $k_{on}$ and $k_{off}$, respectively. In the cytosol, Ect2 can get phosphorylated enzymatically with a rate $k_{[Cdk1]}$, which we describe by Michaelis–Menten kinetics with a Michaelis–Menten constant $K_p$. Furthermore, Ect2 can get dephosphorylated with a rate $k_{dp}$. As bistability typically arises from feedback loops in the reaction kinetics, we include a feedback loop such that active Ect2 enhances its own activation with a rate $k_{fb}$.

*Parameters for the Ect2 module.* The parameters of this model are specified in Supplementary Table 2. The reaction rates represent effective rates that can depend on the concentration of other proteins. These rates are chosen such that the model exhibits a bistable window for a range for phosphorylation rates (Cdk1 concentrations). The diffusion constants are chosen such that the diffusion constant in the cytosol is much larger than the diffusion constant on the membrane ($D_c \gg D_m$). The ratio of the Cdk1 decay rate to the Cdk1 slope can be estimated from the surface contraction wave propagation speed (10–35 μm min$^{-1}$).

To emulate the effect of the Cdk1 gradient, we assume that the Cdk1-dependent phosphorylation rate $k_{[Cdk1]}(\mathbf{r}, t)$ is a decaying linear gradient:

$$k_{[Cdk1]}(r, t) = (c_0 - \alpha r)\left(1 - \frac{t}{\gamma + t}\right).$$

Here, $\gamma$ is the Cdk1 concentration half-life and $c_0$ and $\alpha$ are the maximum and slope of the gradient, respectively. As an initial condition, we assume that Ect2 is in the phosphorylated state such that $u_{Ep} = n_E$ and $u_e = u_E = 0$.

*Reaction–diffusion equations for the Rho module.* We consider a model in which the Rho GTPase diffuses on the surface of a three-dimensional (3D) volume and can cycle between three conformations: an inactive (GDP-bound) cytosolic conformation close to the membrane (concentration $u_R(\mathbf{r}, t)$), an inactive state on the membrane (concentration $u_{rd}(\mathbf{r}, t)$) and an active (GTP-bound) conformation on the membrane (concentration $u_{rt}(\mathbf{r}, t)$). We consider only the cytosolic concentration close to the membrane, assuming the absence of cytosol gradients normal to the membrane. The corresponding reaction–diffusion equations are given by

$$\begin{aligned}\partial_t u_R &= D_R\nabla^2 u_R + f_R(u_R, u_{rd}, u_{rt}),\\ \partial_t u_{rd} &= D_{rd}\nabla^2 u_{rd} + f_{rd}(u_R, u_{rd}, u_{rt}),\\ \partial_t u_{rt} &= D_{rt}\nabla^2 u_{rt} + f_{rt}(u_R, u_{rd}, u_{rt}),\end{aligned}$$

where Rho in the cytosolic state diffuses with a diffusion constant $D_R$, which is much higher than the diffusion constants of the membrane-bound states, $D_{rd}$ and $D_{rt}$. For the reaction kinetics, we assume a generic GTPase reaction cycle, with the reaction terms

$$\begin{aligned}f_R &= k_{off}u_{rd} - k_{on}u_R + k_{gap}u_{rt},\\ f_{rd} &= k_{on}u_R - k_{off}u_{rd} - (k_r + k_{dt}u_{rt}^2)u_{rd},\\ f_{rt} &= (k_r + k_{dt}u_{rt}^2)u_{rd} - k_{gap}u_{rt}.\end{aligned}$$

These reaction kinetics conserve total protein mass, such that $\int_\Omega d\mathbf{r}(u_R + u_{rd} + u_{rt}) = n_R$, where $\Omega$ denotes the computational domain (here the surface of a 3D cytosolic volume). The inactive Rho conformation can attach to and detach from the membrane with rates $k_{on}$ and $k_{off}$, respectively. On the membrane, the inactive conformation can get activated with the basal activation rate $k_r$ and the autocatalytic activation rate $k_{dt}$. Upon hydrolysis of the active state, Rho detaches from the membrane with a rate $k_{gap}$.

*Parameters for the Rho module.* The parameters of this model are specified in Supplementary Table 1. Diffusion constants are chosen such that diffusion in the cytosol is much faster than diffusion on the membrane ($D_R \gg D_{rd}, D_{rt}$). The reaction rates of this model represent effective rates and may depend on the concentration of other regulatory proteins that are not explicitly accounted for in our minimal model. To reproduce the experimental observations, we choose the rate constants such that the reaction kinetics are excitable. A detailed motivation for the parameter is presented in Supplementary Sections 2.6 and 2.7.

To emulate the concentration profile of the propagating Ect2 front, we use a propagating front $\xi_{Ect2} = 0.01 + 0.99\Theta(r - (r_0 - V_{Ect2}t))$, where $r_0$ is the initial front position and $V_{Ect2}$ is the front speed. We multiply the emulated Ect2 front $\xi_{Ect2}$ with the activation rates $k_r$ and $k_{dt}$. This was done for the simulations shown in Fig. 3f,k and Supplementary Videos 14 and 18. Note that one can also use $\xi_{Ect2} = u_e(\mathbf{r}, t) + u_E(\mathbf{r}, t)$, which couples the concentration profile of active Ect2 of the Ect2 module to the Rho module of the model. The latter was used for the simulation in elliptical, triangular and star geometries in Supplementary Videos 15–17.

*Simulation methods, geometry and domain size.* The simulations presented in Fig. 3f,k, Supplementary Fig. 17c and Supplementary Videos 14 and 18 are finite element simulations on the surface of a 3D volume, implemented in COMSOL Multiphysics version 5.4 and with parameters as in Supplementary Table 1. The simulations presented in Fig. 4f–h and Supplementary Videos 15–17 are finite element simulations on the surfaces of 3D ellipsoidal-, triangular- and star-shaped domains, with parameters as in Supplementary Tables 1 and 2. Here, the Rho and Ect2 dynamics are constrained to the surfaces of the static 3D geometries, whereas the Cdk1 concentration is modelled as a linear gradient in the 3D bulk, which extends radially from the position of the nucleus into the cytoplasm.

**Reporting Summary.** Further information on research design is available in the Nature Research Reporting Summary linked to this article.

## Data availability

All data that support the plots within this paper and other findings of this study are available from the corresponding author upon reasonable request.

## Code availability

The code that supports the plots within this paper are described in the Methods and Supplementary Information and are available from the corresponding author upon reasonable request.

## References

42. Benink, H. A. & Bement, W. M. Concentric zones of active RhoA and Cdc42 around single cell wounds. *J. Cell Biol.* **168**, 429–439 (2005).
43. Su, K.-C., Bement, W. M., Petronczki, M. & von Dassow, G. An astral simulacrum of the central spindle accounts for normal, spindle-less, and anucleate cytokinesis in echinoderm embryos. *Mol. Biol. Cell* **25**, 4049–4062 (2014).
44. Gökirmak, T. et al. Localization and substrate selectivity of sea urchin multidrug (MDR) efflux transporters. *J. Biol. Chem.* **287**, 43876–43883 (2012).

## Acknowledgements

We thank P. Lenart, J. Bischof, K. Keren, A. Martin, A. Goryachev and E. Zanin for discussions. We also thank W. Salmon and staff at the W.M. Keck Microscopy Facility at the Whitehead Institute for microscopy support. E.F. acknowledges the hospitality of the Kavli Institute of Nanoscience at the Delft University of Technology where part of this work was done. This research was supported by a National Science Foundation CAREER award (to N.F.), a German Research Foundation (Deutsche Forschungsgemeinschaft, DFG) fellowship within the Graduate School of Quantitative Biosciences Munich (to M.C.W.), the Joachim Herz Foundation (to M.C.W.), the DFG via B2 projects within the Collaborative Research Center SFB 1032 (to E.F.), and the DFG via the Research Training Group GRK 2062 (to F.B.). This research was supported in part by the National Science Foundation under grant no. NSF PHY-1748958.

## Author contributions

T.H.T. and N.F. initiated the project and designed the experiments. T.H.T. and J.L. performed the experiments and analysed the experimental data. M.C.W., F.B. and E.F. designed the model. M.C.W. performed the simulations and analysed the simulation data. S.Z.S. contributed reagents. All authors participated in interpreting the experimental and theoretical results and in writing the manuscript.

## Competing interests

The authors declare no competing interests.

## Additional information

**Supplementary information** The online version contains supplementary material available at https://doi.org/10.1038/s41567-021-01164-9.

**Correspondence and requests for materials** should be addressed to E.F. or N.F.

**Peer review information** *Nature Physics* thanks Leah Edelstein-Keshet, Nicolas Minc and the other, anonymous, reviewer(s) for their contribution to the peer review of this work.

**Reprints and permissions information** is available at www.nature.com/reprints.

nature research

Corresponding author(s): Nikta Fakhri, Erwin Frey

Last updated by author(s): Feb 10, 2020

# Reporting Summary

Nature Research wishes to improve the reproducibility of the work that we publish. This form provides structure for consistency and transparency in reporting. For further information on Nature Research policies, see Authors & Referees and the Editorial Policy Checklist.

## Statistics

For all statistical analyses, confirm that the following items are present in the figure legend, table legend, main text, or Methods section.

| n/a | Confirmed | |
|---|---|---|
| ☐ | ☒ | The exact sample size (*n*) for each experimental group/condition, given as a discrete number and unit of measurement |
| ☐ | ☒ | A statement on whether measurements were taken from distinct samples or whether the same sample was measured repeatedly |
| ☒ | ☐ | The statistical test(s) used AND whether they are one- or two-sided<br>*Only common tests should be described solely by name; describe more complex techniques in the Methods section.* |
| ☒ | ☐ | A description of all covariates tested |
| ☒ | ☐ | A description of any assumptions or corrections, such as tests of normality and adjustment for multiple comparisons |
| ☒ | ☐ | A full description of the statistical parameters including central tendency (e.g. means) or other basic estimates (e.g. regression coefficient) AND variation (e.g. standard deviation) or associated estimates of uncertainty (e.g. confidence intervals) |
| ☒ | ☐ | For null hypothesis testing, the test statistic (e.g. *F*, *t*, *r*) with confidence intervals, effect sizes, degrees of freedom and *P* value noted<br>*Give P values as exact values whenever suitable.* |
| ☒ | ☐ | For Bayesian analysis, information on the choice of priors and Markov chain Monte Carlo settings |
| ☒ | ☐ | For hierarchical and complex designs, identification of the appropriate level for tests and full reporting of outcomes |
| ☒ | ☐ | Estimates of effect sizes (e.g. Cohen's *d*, Pearson's *r*), indicating how they were calculated |

*Our web collection on statistics for biologists contains articles on many of the points above.*

## Software and code

Policy information about availability of computer code

| | |
|---|---|
| Data collection | Zeiss confocal LSM 700 and LSM 710 used to collect data is operated using Zen software. |
| Data analysis | All experimental data analyses is done using a custom code written in Matlab, which will be available upon request. The model and parameter choices to generate the theoretical results are available in the Supplementary Materials. |

For manuscripts utilizing custom algorithms or software that are central to the research but not yet described in published literature, software must be made available to editors/reviewers. We strongly encourage code deposition in a community repository (e.g. GitHub). See the Nature Research guidelines for submitting code & software for further information.

## Data

Policy information about availability of data

All manuscripts must include a data availability statement. This statement should provide the following information, where applicable:

- Accession codes, unique identifiers, or web links for publicly available datasets
- A list of figures that have associated raw data
- A description of any restrictions on data availability

All data needed to evaluate the conclusions in the paper are present in the paper and/or the Supplementary Materials.

# Field-specific reporting

Please select the one below that is the best fit for your research. If you are not sure, read the appropriate sections before making your selection.

☒ Life sciences ☐ Behavioural & social sciences ☐ Ecological, evolutionary & environmental sciences

# Life sciences study design

All studies must disclose on these points even when the disclosure is negative.

| | |
|---|---|
| Sample size | For Rho imaging, more than 20 oocytes in various geometries (as specified in paper) were recorded.<br>For Cdk1 imaging, more than 10 oocytes in various geometries were recorded.<br>Each experimental plot (1d, 3g and 4h-i) consist of data points from at least 10 oocytes. |
| Data exclusions | Oocytes which did not complete meiosis I and which did not show sufficient expression of fluorescent markers are excluded from the study. |
| Replication | All experimental plots and imaging results (Rho and Cdk1 kymographs) consist of data from at least 3 different experiments, which show consistent results. |
| Randomization | Not relevant to study. |
| Blinding | Not relevant to study. |

# Reporting for specific materials, systems and methods

We require information from authors about some types of materials, experimental systems and methods used in many studies. Here, indicate whether each material, system or method listed is relevant to your study. If you are not sure if a list item applies to your research, read the appropriate section before selecting a response.

## Materials & experimental systems

| n/a | Involved in the study |
|---|---|
| ☒ | ☐ Antibodies |
| ☒ | ☐ Eukaryotic cell lines |
| ☒ | ☐ Palaeontology |
| ☐ | ☒ Animals and other organisms |
| ☒ | ☐ Human research participants |
| ☒ | ☐ Clinical data |

## Methods

| n/a | Involved in the study |
|---|---|
| ☒ | ☐ ChIP-seq |
| ☒ | ☐ Flow cytometry |
| ☒ | ☐ MRI-based neuroimaging |

## Animals and other organisms

Policy information about studies involving animals; ARRIVE guidelines recommended for reporting animal research

| | |
|---|---|
| Laboratory animals | Patiria Miniata |
| Wild animals | Wild starfish Patiria Miniata was procured from South Coast Bio-Marine LLC. The animals were kept in salt water fish tank maintained at 15 °C. Due to their wound healing capacity, multiple rounds of oocytes harvesting can be done without sacrificing the starfish. |
| Field-collected samples | Not relevant for study. |
| Ethics oversight | No ethical requirement since the animal is invertebrate. |

Note that full information on the approval of the study protocol must also be provided in the manuscript.